

Supporting Information for < Effects of microfractures on permeability in carbonate rocks based on digital core technology >

Changfu Liu^{1,2}, Li Zhang³, Yongchen Li⁴, Fugui Liu^{1,2}, Dmitriy A. Martyushev⁵,
Yongfei Yang^{1,2*}

¹ Key Laboratory of Unconventional Oil & Gas Development (China University of Petroleum (East China)), Ministry of Education, Qingdao 266580, P.R. China

² School of Petroleum Engineering, China University of Petroleum (East China), Qingdao 266580, P.R. China.

³ Geological Exploration & Development Research Institute, CNPC Chuanqing Drilling Engineering Company Limited, Chengdu 610051, P. R. China

⁴ PetroChina Coalbed Methane Company Limited, Beijing 100028, P. R. China.

⁵ Department of Oil and Gas Technologies, Perm National Research Polytechnic University, Perm 614990, Russia

This file includes:

- Materials and Methods
- Supplemental Text
- Figs. S1 to S10
- Table S1
- References

1 Material and methods

1.1 Digital cores with fractures

The digital rocks used in this paper were acquired from CT scans of real carbonate rocks. The CT equipment used in our experiment was a Zeiss MicroXCT-400 machine. CT technology uses X-rays to penetrate the sample, receives the signal after radiation attenuation by the detector, and then uses the X-ray attenuation equation to invert the density distribution information of the detected object. With the help of CT scans and image processing technology, the qualitative and quantitative analysis of the object can be completed. The X-ray attenuation from the CT source satisfies the Beer-Lambert law:

$$I = I_0 e^{-\sum_i \mu_i x_i} \quad (1)$$

where I_o and I are the intensity of the X-ray before and after it passes through the object; μ_i is the attenuation coefficient of component i to X-ray, and x_i is the length of the component in the current path of X-ray.

After CT scanning, the 3D grayscale data composed of a series of 2D slices were obtained, and the digital cores were built via image processing such as subvolume extraction, noise reduction by filtering, and segmentation (Andrä et al., 2013). We chose two types of carbonates to study the effect of microfractures on permeability. The 2D slices of two rocks are shown in Fig. S1, where S1 has obvious small caves, and the pore size of S2 is larger. To add different microfractures to digital cores, subvolumes were extracted from two carbonate rocks, as shown in Fig. S2. The acquired subvolume size is $200 \times 200 \times 200$ voxels, the voxel size is $4.32\mu\text{m}$. Thus, the actual physical size is $864 \mu\text{m} \times 864 \mu\text{m} \times 864 \mu\text{m}$. By extracting the pore network models of digital cores (Yang et al., 2019), the quantitative pore structure characteristics were obtained in Table S1. Compared with S1, S2 has larger average pore radius, throat radius, and coordination number, thus exhibiting better porosity and permeability.

The representative digital core was used as the basis to add microfracture, the fracture system had the same size as the subvolume so that the superposition of the two systems can be completed (Wang et al., 2013). Finally, the two systems were integrated and the digital cores with different fracture properties could be used in the permeability calculation. The structural characteristics of microfractures mainly include length (L_f), aperture (W_f), angle (θ_f), and density (N), in which the angle of fractures represents the angle between the direction of fractures and seepage flow, the density represents fracture number in a digital core.

1.2 Lattice Boltzmann method

In this paper, a D3Q19 discrete velocity model is applied to simulate the permeability of three-dimensional digital cores. Lattice Bhatnagar-Gross-Krook (LBGK) collision approximation has been widely used for its simplicity (Qian et al., 1992; Pradipto and Purqon, 2017). The basic evolution equation is as follows:

$$f_i(r + e_i \Delta t, t + \Delta t) - f_i(r, t) = -\frac{1}{\tau} (f_i - f_i^{eq}) \quad (2)$$

where f_i and f_i^{eq} are the distribution function and equilibrium distribution function in i direction ($i = 0, 1, 2, \dots, 18$) respectively; r represents the spatial position of a node;

t and Δt are the time and time step respectively; τ is the relaxation time, which represents the average time interval between two collisions and is defined as follows:

$$\tau = \frac{\nu}{c_s^2 \Delta t} + 0.5 \quad (3)$$

where ν is the fluid viscosity; c_s is the lattice sound velocity and $c_s = \frac{1}{\sqrt{3}}$ (Arumuga Perumal and Dass, 2015).

For the D3Q19 model, the equilibrium distribution function is:

$$f_i^{eq} = w_i \left[\rho + \rho_0 \left(3(e_i \cdot u) + \frac{9(e_i \cdot u)^2}{2} - \frac{3u^2}{2} \right) \right] \quad (4)$$

where w_i is the weight coefficient in i direction, which is expressed as:

$$w_i = \begin{cases} 1/3 & i = 0 \\ 1/18 & i = 1, 2, \dots, 6 \\ 1/36 & i = 7, 8, \dots, 18 \end{cases} \quad (5)$$

In this model, the macroscopic density ρ , velocity u and pressure p are defined as:

$$\rho = \sum_{i=1}^{18} f_i \quad (6)$$

$$u = \frac{1}{\rho} \sum_{i=1}^{18} f_i e_i \quad (7)$$

$$p = c_s^2 \rho \quad (8)$$

When the permeability of the digital core is calculated, the wall surface is usually modeled as a non-slip boundary condition. The rebound scheme is a common scheme for dealing with non-slip boundaries. Fluid particles will return the pore space along the original path if they reach the wall surface (Zou and He, 1997). Since the fluid flow is driven by pressure, periodic pressure boundary conditions are set at the left and right boundaries, setting a fixed pressure gradient of 0.00005. It should be noted that all the variables are dimensionless lattice units. During the flow simulation, if the difference in the macroscopic velocity of the fluid is less than 10^{-6} between two adjacent times, the system has reached equilibrium and the simulation is terminated. At this point, the

macroscopic flow rate can be calculated by integrating the area of the flow rate at each node on the outlet.

$$U = \sum_y \sum_z (u \cdot R_e^2) \quad (9)$$

where R_e represents the image resolution. According to Darcy's law, the equivalent permeability of digital cores with fractures can be calculated as Equation(10), the permeability of two carbonates obtained by LBM is listed in

$$-\frac{dP}{dx} = \frac{\mu}{k} U \quad (10)$$

2 Supplemental Text

2.1 Effects of different fracture length

To investigate the effect of fracture length on the seepage characteristics, S1 and S2 of which the length L is 200 lattice units were selected by comparing the permeability with fracture k_f and initial matrix permeability k . Microfractures with different lengths were added to each of the two digital cores to build a dual fracture-pore system. The fracture length L_f extends along the flow direction, while the fracture aperture, angle, and fracture number are the constant 4, 0° , and 1, respectively.

For S1 in Fig. S3, the fracture does not fully participate in the seepage process when the fracture length is short. The primary reason is that the matrix pores of this digital core are not as good as S2 and fewer pores are connected to the fracture, which results in the limited enhancement of the seepage performance. And as the fracture length increases, the main seepage channels are formed in the fracture, and the overall seepage velocity is significantly larger than that in the digital core with short fracture.

For the dual fracture-pore system in S2, as seen from Fig. S4, when the fracture length is short, more matrix pores are involved in the percolation. In addition, there are larger percolation velocities in the pores apart from the fracture, indicating that the effect of the fracture on the matrix permeability is not yet obvious. Then, as the fracture length increases, more pores are contributed to fluid flow.

2.2 Effects of different fracture aperture

To investigate the effect of fracture aperture on the seepage characteristics, the fracture length is 100, the angle is 0° , and the number of fractures is set to 1. The selected fracture apertures are 1, 2, 3, 4, and 5, respectively.

Fig. S5 and Fig. S6 represent the velocity field distributions of two cores with different fracture apertures at a fracture length of 100 lattice units in the dual fracture-pore system. The middle part of the streamline is relatively sparse, but with the increase of fracture aperture, streamlines become denser. This indicates that the increase of fracture aperture enhances the flow capacity. Compare (b) and (d) in Fig. S5 and Fig. S6, it can be found that with the increase of the fracture aperture, the flow velocity in the fracture and the pore connected with the fracture is significantly increased. In addition, as the aperture increases, no new seepage channels are formed. This is because the aperture is generally much smaller than the length, the effect of increasing aperture on enhancing the connectivity of the whole core is not obvious.

According to the analysis in the previous section, the fractures have different effects on permeability when the fracture length is different. For the fracture that connects the two boundaries of the core ($L_f/L = 1$), the LBM flow simulation was performed, and the results are shown in Fig. S7 and Fig. S8, the flow capacity at this time depends entirely on the fracture.

2.3 Effects of different fracture density

To investigate the effect of fracture density on the seepage characteristics, the fracture length is 100, the aperture is 2, the angle is 0° . The selected fracture numbers are set to 1, 2, 3, 4, and 5, respectively.

The three-dimensional velocity field distribution obtained by LBM with different fracture numbers is shown in Fig. S9 and Fig. S10. The seepage channels are formed in each fracture. As the number of fractures increases, the density of streamlines increases. This indicates that there are more pores involved in the seepage, expanding the seepage space, and thus enhancing the overall seepage capacity.

2.4 Effects of different fracture angle

To investigate the effect of fracture angle on the seepage characteristics, the fracture length is 100, the aperture is 4, the fracture number is 1. The selected fracture angles are set to 0° , 30° , 45° , 60° , and 90° , respectively. When the angle is 90° , the fracture direction is perpendicular to the flow direction.

The three-dimensional velocity field distribution obtained by LBM with different fracture angles is shown in Fig. S11 and Fig. S12. Due to the change of fracture angle, the collocation relationship between fractures and pores is changed, which leads to the change of seepage channels. And the number of streamlines decreases with the increase

of fracture angle, which indicates that the flow channels appear to decrease. However, there is no obvious change in seepage velocity in pores and fractures.

3 Figures and Table

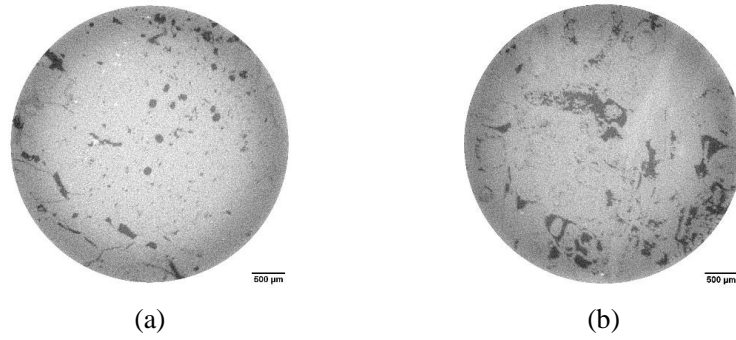


Fig. S1 2D Slices of two carbonate rocks obtained by X-ray CT: (a) S1 and (b) S2.

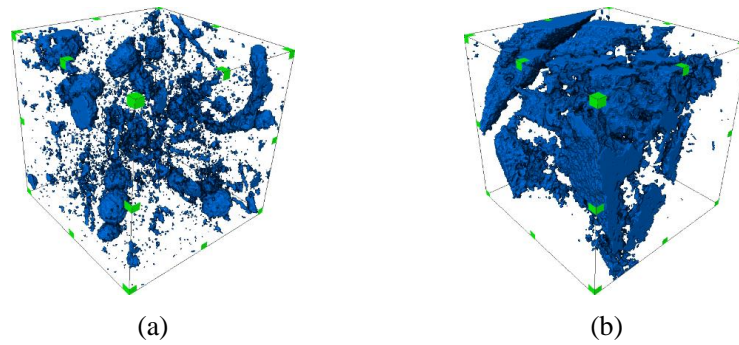
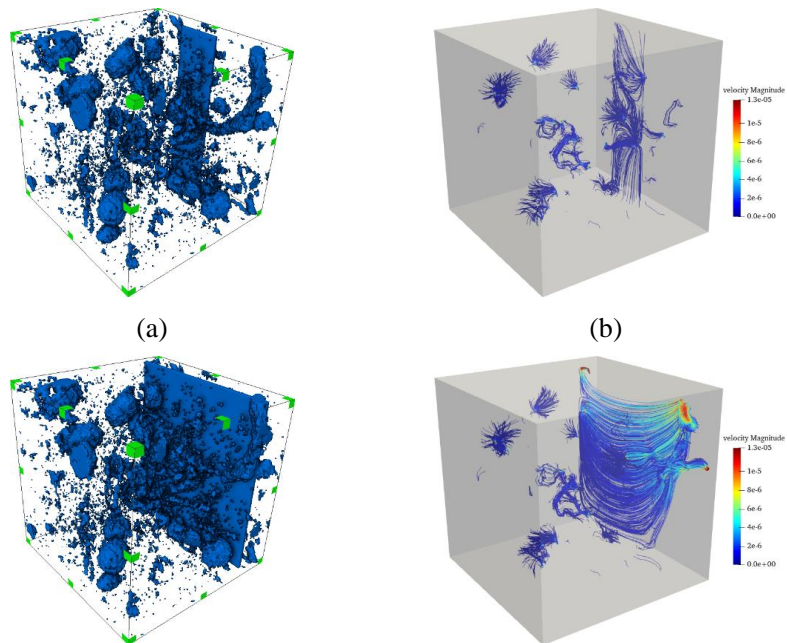


Fig. S2 Digital core of two carbonate rocks (the blue region is pore space): (a) S1 and (b) S2.



(c) (d)
Fig. S3 Digital core and velocity field distribution of S1 with different fracture length: (a) and (c) represent the system with $L_f/L = 0.25$ and $L_f/L = 0.9$ respectively; (b) and (d) represent the velocity field distribution with $L_f/L = 0.25$ and $L_f/L = 0.9$ respectively.

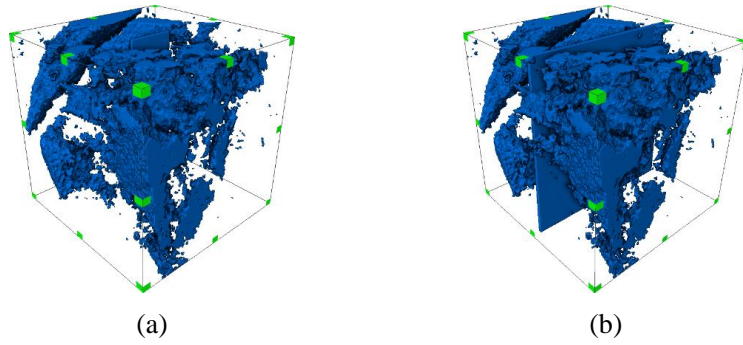


Fig. S4 Digital core of S2 with different fracture length: (a) and (b) represent the system with $L_f/L = 0.25$ and $L_f/L = 0.9$ respectively

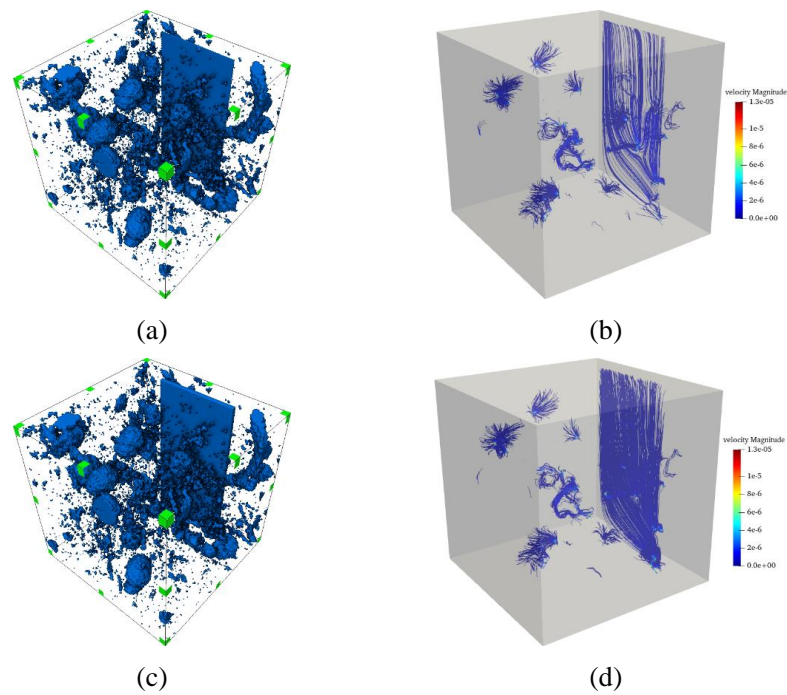


Fig. S5 Digital core and velocity field distribution of S1 with different fracture aperture ($L_f/L = 0.5$): (a) and (c) represent the system with $W_f = 1$ and $W_f = 5$ respectively; (b) and (d) represent the velocity field distribution with $W_f = 1$ and $W_f = 5$ respectively.

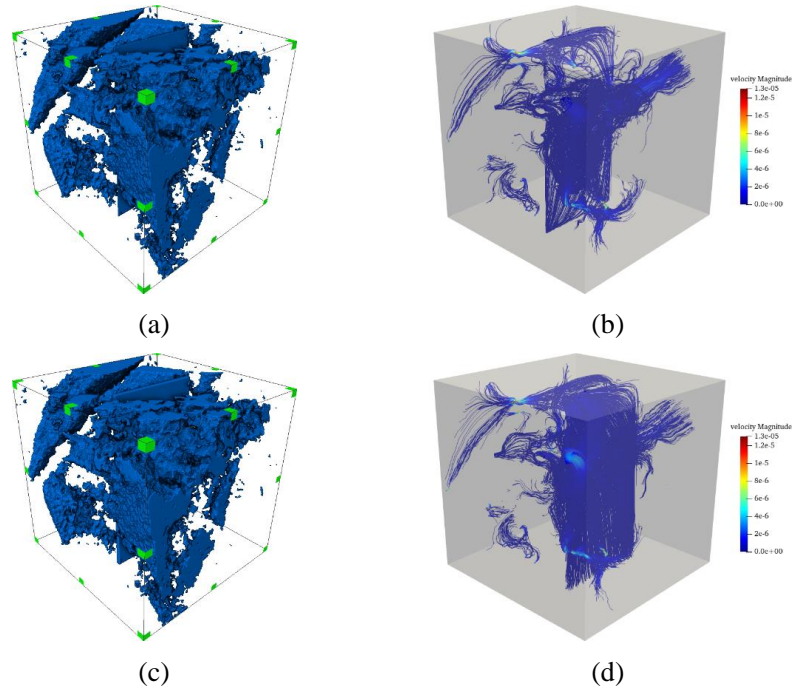


Fig. S6 Digital core and velocity field distribution of S2 with different fracture aperture ($L_f/L = 0.5$): (a) and (c) represent the system with $W_f = 1$ and $W_f = 5$ respectively; (b) and (d) represent the velocity field distribution with $W_f = 1$ and $W_f = 5$ respectively.

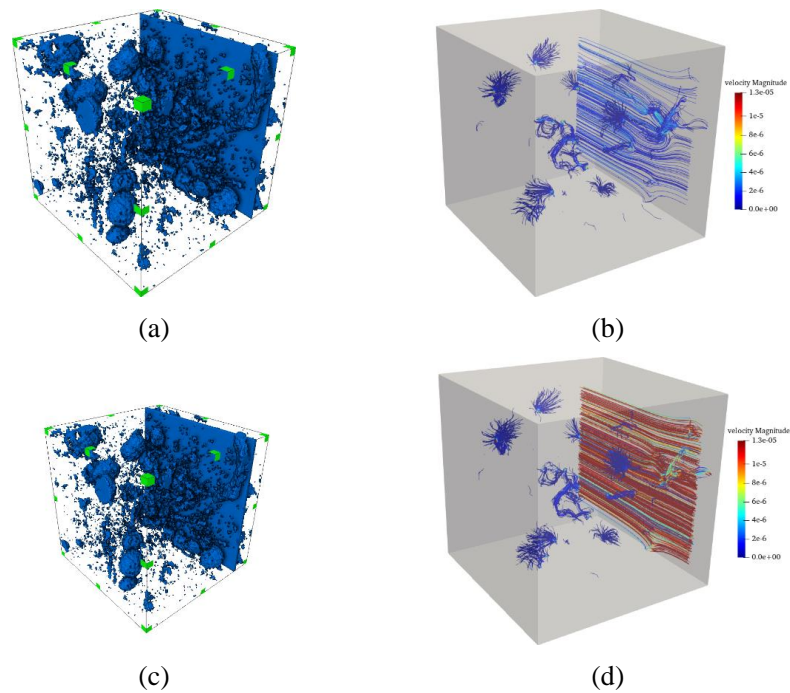


Fig. S7 Digital core and velocity field distribution of S1 with different fracture aperture ($L_f/L = 1$): (a) and (c) represent the system with $W_f = 1$ and $W_f = 5$ respectively; (b) and (d) represent the velocity field distribution with $W_f = 1$ and $W_f = 5$ respectively.

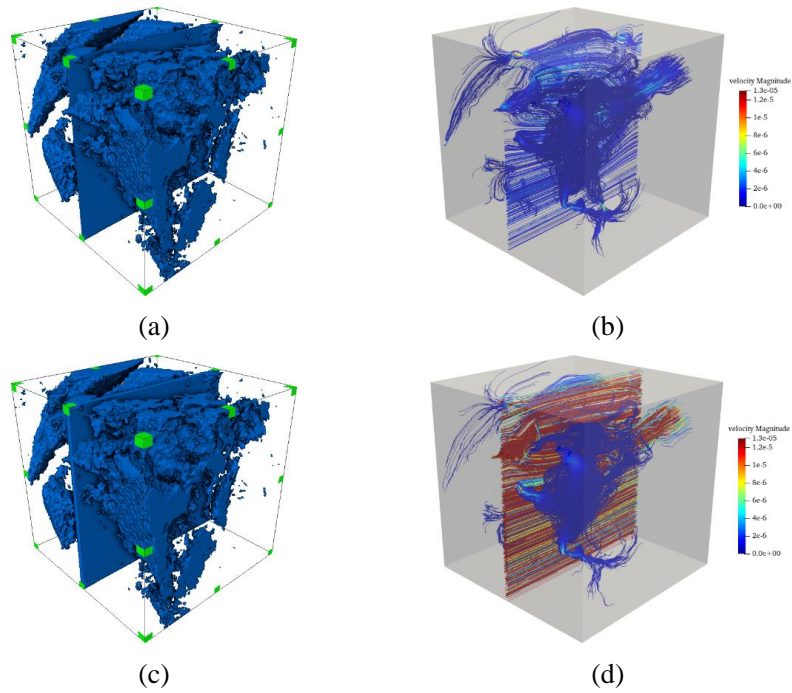


Fig. S8 Digital core and velocity field distribution of S2 with different fracture aperture ($L_f/L = 1$): (a) and (c) represent the system with $W_f = 1$ and $W_f = 5$ respectively; (b) and (d) represent the velocity field distribution with $W_f = 1$ and $W_f = 5$ respectively.

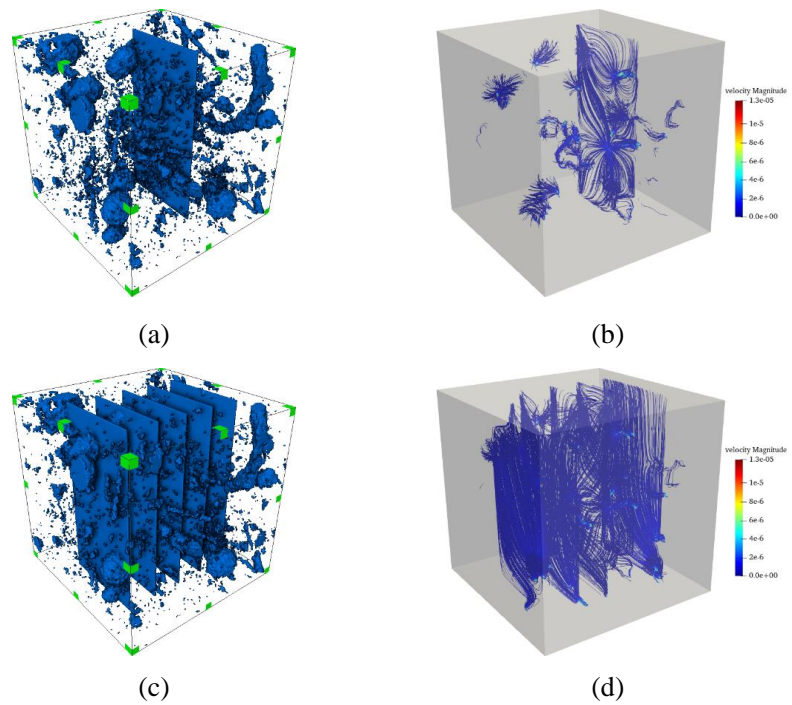


Fig. S9 Digital core and velocity field distribution of S1 with different fracture density: (a) and (c) represent the system with 1 and 5 fractures respectively; (b) and (d) represent the velocity field distribution with 1 and 5 fractures respectively.

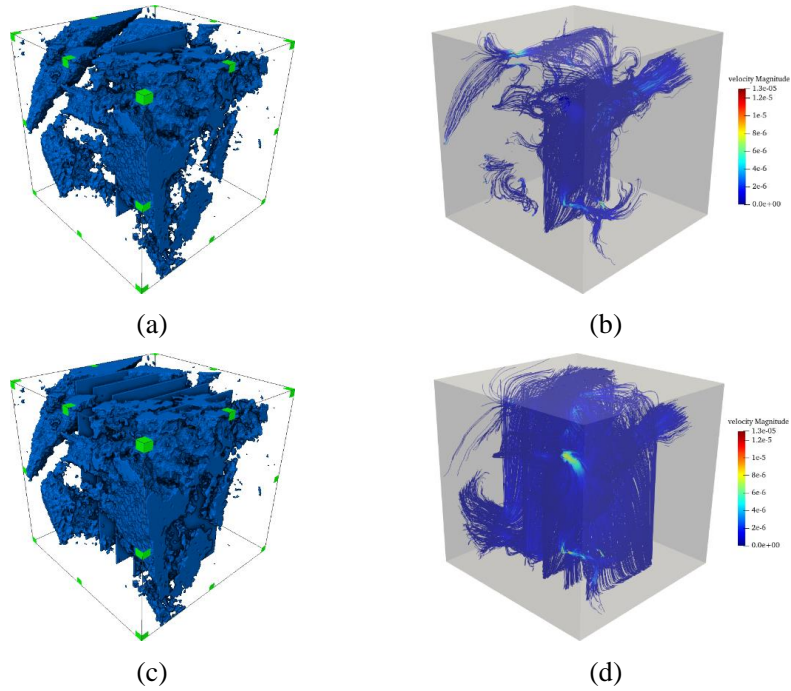


Fig. S10 Digital core and velocity field distribution of S2 with different fracture density: (a) and (c) represent the system with 1 and 5 fractures respectively; (b) and (d) represent the velocity field distribution with 1 and 5 fractures respectively.

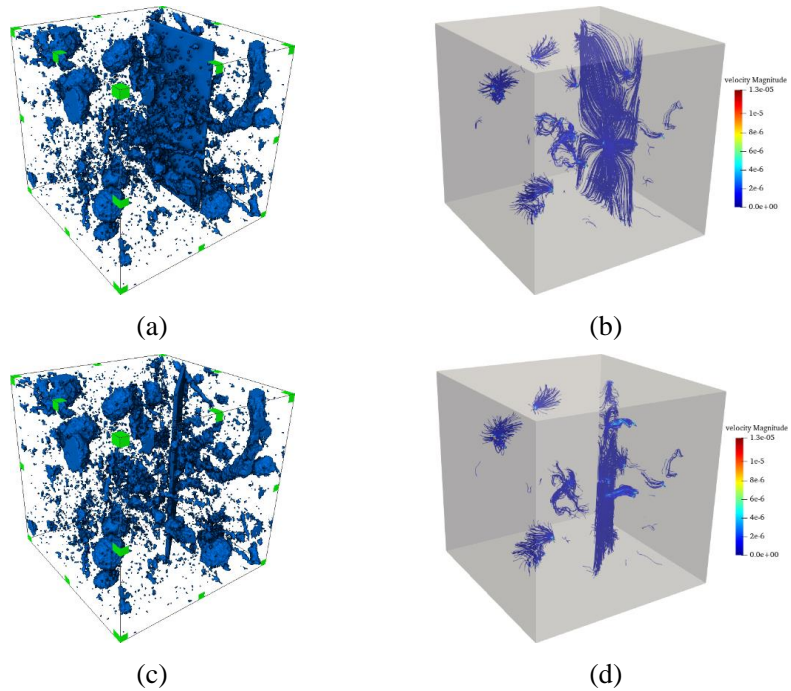


Fig. S11 Digital core and velocity field distribution of S1 with different fracture angle: (a) and (c) represent the system with fractures of 0° and 45° respectively; (b) and (d) represent the velocity field distribution with fractures of 0° and 45° respectively.

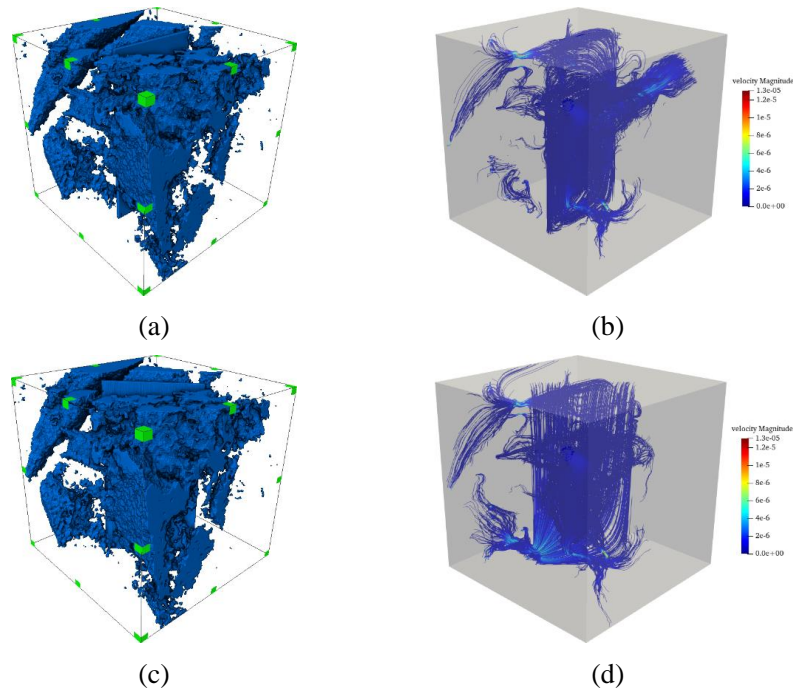


Fig. S12 Digital core and velocity field distribution of S2 with different fracture angle: (a) and (c) represent the system with fractures of 0° and 45° respectively; (b) and (d) represent the velocity field distribution with fractures of 0° and 45° respectively.

Table S1 The parameters of the extracted digital core.

	S1	S2
Porosity (%)	3.53	8.81
Permeability (mD)	2.81	9.588
Average pore radius (μm)	9.73	11.35
Average throat radius (μm)	7.05	9.81
Average coordination number	2.47	3.54
Average tortuosity	4.32	3.73

References

- Andrä, H., Combaret, N., Dvorkin, J., et al. Digital rock physics benchmarks—part i: Imaging and segmentation. *Computers & Geosciences* 2013, 50: 25-32.
- Arumuga Perumal, D., Dass, A.K. A review on the development of lattice Boltzmann computation of macro fluid flows and heat transfer. *Alexandria Engineering Journal* 2015, 54(4): 955-971.
- Pradipto, Purqon, A. Accuracy and numerical stability analysis of lattice Boltzmann method with multiple relaxation time for incompressible flows. *Journal of Physics: Conference Series* 2017, 877: 012035.

Qian, Y.H., D'Humières, D., Lallemand, P. Lattice bgk models for navier-stokes equation. *Europhysics Letters (EPL)* 1992, 17(6): 479-484.

Wang, X., Yao, J., Yang, Y.F., et al. Permeability prediction in digital core with curved fractures based on combined plate model. *Zhongguo Shiyou Daxue Xuebao (Ziran Kexue Ban)/Journal of China University of Petroleum (Edition of Natural Science)* 2013, 37(6): 82-86. (in Chinese)

Yang, Y., Wang, K., Zhang, L., et al. Pore-scale simulation of shale oil flow based on pore network model. *Fuel* 2019, 251: 683-692.

Zou, Q., He, X. On pressure and velocity boundary conditions for the lattice Boltzmann BGK model. *Physics of Fluids* 1997, 9(6): 1591-1598.